Diffusion-induced phase transformations across the γ-loop in the Fe–Cr system

Journal of Alloys and Compounds 1080 (2026) 190430

Contents lists available at ScienceDirect

Journal of Alloys and Compounds

journal homepage: www.elsevier.com/locate/jalcom

Diffusion-induced phase transformations across the γ-loop in the Fe–Cr system

Anton Chyrkin

Chalmers University of Technology, Department of Chemistry and Chemical Engineering, Kemivägen 10, Gothenburg 412 58, Sweden

ARTICLE INFO

Keywords:
Interdiffusion
Fe-Cr
Ferritic steels
Ferrite
Austenite
Phase transformation
Oxidation
Cr-depletion
CALPHAD modeling
Wagner theory

ABSTRACT

Interdiffusion and diffusion-induced phase transformations around the γ-loop in the Fe–Cr system were investigated using diffusion couples between Fe–Cr alloys (10 and 18 wt% Cr) and pure Fe at 800–1000 °C. New phase layers form when the diffusion path intersects the γ-loop. At 1000 °C, a ferrite layer grows into the austenitic Fe–10Cr side, whereas at 900 °C, an austenitic layer forms in the initially ferritic Fe–18Cr / Fe couple. DICTRA simulations accurately reproduce concentration profiles, phase distributions, and interface positions without adjustable parameters. Classical Wagner-type analysis quantitatively reproduces interdiffusion coefficients in both BCC and FCC phases based on the measured phase growth kinetics. The results provide direct experimental evidence of diffusion-induced α→γ transformation driven by chromium depletion and establish its role in accelerated oxidation of Fe–Cr alloys at 900 °C and above.

1. Introduction

Ferritic stainless steels (FSS) [1,2], based on the Fe–Cr system with typical chromium contents of 12–18 wt% (up to ~30 wt% in some grades), are widely used in high-temperature applications due to their ability to form slow-growing, electrically conductive chromia (Cr_2O_3) scales. These properties make them attractive for application in solid oxide fuel cells (SOFCs) [3,4] and solid oxide electrolysis cells (SOECs) [5,6] as interconnect materials [4], as well as in heat exchangers [7], automotive exhaust systems [7,8], catalytic converter substrates, and chemical and petrochemical processing equipment operating in corrosive and oxidizing environments.

The oxidation resistance of Fe–Cr alloys relies on the selective oxidation of chromium to form a continuous Cr_2O_3 scale [9,10]. However, this process is strongly impaired in the presence of water vapor [11,12]. In alloys with intermediate chromium contents (10–20 wt%), this often results in breakaway oxidation, characterized by the formation of Fe-rich oxide scales and internal oxidation, leading to oxidation rates several orders of magnitude higher than in dry environments. Despite extensive study, the mechanisms underlying the detrimental influence of water vapor remain debated. Proposed explanations include chromium volatilization [13–15], modification of defect transport in Cr_2O_3 by hydrogen-related species [16,17], preferential adsorption of H_2O [11], and enhanced oxygen permeability associated with hydrogen [18–20]. Conflicting results indicate that the role of hydrogen and water vapor at intermediate temperatures around 600 °C is not yet fully resolved.

At temperatures above 850 °C, additional degradation phenomena associated with accelerated oxidation have been reported since the late 1960s [21–23]. This Cr depletion may induce phase transformations from α-ferrite to γ-austenite [24–26], potentially altering Cr diffusion and affecting chromia scale stability. However, experimental evidence directly linking oxidation-induced chromium depletion to austenite formation remains lacking.

The Fe–Cr system [27], which forms the basis of ferritic and ferritic–martensitic steels, is among the most extensively studied alloy systems in terms of both thermodynamics and diffusion kinetics. Phase equilibria [27,28] and diffusion coefficients in the individual α (BCC) and γ (FCC) phases have been determined in numerous experimental studies, including tracer diffusion [29–31] and diffusion couple investigations [32,33], and are well described within CALPHAD-type assessments. Despite this mature understanding, available studies are almost exclusively limited to diffusion within single-phase regions. Interdiffusion across the α/γ phase boundary involving the formation of new phases during annealing was previously investigated in the pioneering work of Nishizawa and Chiba [34]. The authors systematically studied ferrite formation in α/γ diffusion couples and during chromium vapor diffusion into austenitic Fe–Cr alloys at 900–1200 °C, providing

E-mail address: chyrkin@chalmers.se.

https://doi.org/10.1016/j.jallcom.2026.190430
Received 6 June 2026; Received in revised form 24 July 2026; Accepted 12 August 2026
Available online 13 August 2026

the first experimental characterization of interfacial migration and non-equilibrium interface compositions. However, the formation of γ-austenite by chromium depletion in initially ferritic alloys outside the γ-loop (e.g., Fe–18Cr at 900–1000 °C) has not been investigated experimentally.

This lack of experimental data is particularly critical in the context of the recently proposed austenitization mechanism of breakaway oxidation [24–26]. This mechanism implies that phase transformations such as α→γ may occur locally and dynamically, potentially governing transport processes and oxidation behavior. Consequently, separating environmental effects from intrinsic diffusion-controlled phase evolution requires a dedicated investigation of interdiffusion across phase boundaries in well-defined model systems free from oxidation.

In this work, phase transformations and interdiffusion in the Fe–Cr system are systematically investigated using diffusion couples between Fe–Cr model alloys (10 and 18 wt% Cr) and pure Fe. Diffusion welded samples were exposed at 800, 900, and 1000 °C, and the resulting microstructures and compositional profiles were characterized by optical light microscopy (LOM), scanning electron microscopy (SEM), and energy-dispersive X-ray spectroscopy (EDX). The experimental results are quantitatively compared with thermodynamic and kinetic simulations performed using Thermo-Calc and DICTRA as well as the classical Wagner theory. By isolating diffusion-driven phase transformations from oxidation effects, this study provides direct experimental and computational evidence of phase evolution across the α/γ phase boundary in Fe–Cr systems at high temperatures. The present approach enables a mechanistic assessment of phase formation induced by interdiffusion, thereby addressing a critical knowledge gap in the experimental validation of phase equilibria and diffusion interactions in the Fe–Cr system.

2. Experimental

2.1. Materials

Binary model alloys Fe–9.98Cr and Fe–18.6Cr (wt%), the ternary alloy Fe–18.3Cr–1.8Mo (wt%), and pure iron were supplied by MWH Hauner GmbH (Röttenbach, Germany). The alloys were produced from pure elements (≥99.995 wt%) by vacuum arc melting. The detailed chemical compositions, determined by inductively coupled plasma optical emission spectroscopy (ICP-OES) and infrared (IR) spectroscopy for C, S, N, and O, are listed in Refs. [24,26]. The impurities of all kinds did not exceed 60 ppm.

The cast ingots, together with pure Fe, were homogenized at 1150 °C for 6 h under vacuum and subsequently hot-rolled into sheets with a thickness of 2.5 mm. The Fe sheet was additionally annealed under flowing Ar–4%H_2 at 1050 °C for 100 h to remove residual FeO from the metallic matrix. The resulting grain size in the Fe specimen was 0.6 mm. The average grain size of the alloys after processing was approximately 50 μm.

Cylindrical specimens with a diameter of 21 mm were machined from the sheets for diffusion couple preparation and subsequently ground to a thickness of 2 mm. In addition, Fe–18Cr and Fe–18Cr–2Mo sheets were cold-rolled to a thickness of 0.6 mm for oxidation experiments. Rectangular specimens (20 × 10 × 0.6 mm^3) were cut from these sheets, ground to a P1200 SiC surface finish, ultrasonically cleaned in acetone and ethanol, and dried in pressurized air prior to exposure.

2.2. Oxidation tests

In-situ oxidation kinetics were measured isothermally using a SETARAM thermobalance in a flowing Ar–4%H_2–7%H_2O gas mixture at 900 °C for up to 72 h. The Ar–4%H_2 gas (Linde Gas) was humidified by passing it through a water bath maintained at 39.1 °C. The resulting oxygen partial pressure at 900 °C was approximately 1.8×10^{-16} bar, which is above the Fe/FeO equilibrium oxygen partial pressure (1.7×10^{-17} bar), thereby allowing external oxidation of Fe. Below this threshold, only internal oxidation, i.e., precipitation of internal Fe–Cr spinel particles, is thermodynamically possible [24]. The values of pO_2 for both the Fe/FeO equilibrium and the H_2/H_2O gas mixture were calculated following the procedure described by Young [35], using the standard enthalpies and entropies of formation tabulated in [36,37].

The heating and cooling rates were 90 K·min^{-1} and 10 K·min^{-1}, respectively. The gas flow in the system was 2 L h^{-1} or 0.2 cm s^{-1}.

2.3. Diffusion welding

Diffusion couples were prepared by diffusion welding using a clamping technique described in Refs. [38,39]. The bonding surfaces of all cylindrical specimens were ground to P4000 SiC finish and subsequently polished with diamond pastes (Struers, Denmark) to 1 μm surface finish.

Two diffusion couple configurations were assembled (Fig. 1):
(i) Fe–18Cr / Fe–10Cr / Fe (DC1),
and (ii) Fe–18Cr / Fe / Fe–18Cr–2Mo (DC2).

The stacked cylinders were placed between two circular flanges (outer diameter 40 mm) made of austenitic 310 L steel and tightened using six screws to ensure good mechanical contact. The assembly was inserted into a quartz tube (inner diameter 43 mm) and heated under flowing Ar–4%H_2 (200 ml·min^{-1}) to 800 °C (DC2), 900 °C (DC2), or 1000 °C (DC1) for 4 h. After welding, the samples were removed from the furnace and cooled in air.

The welded diffusion couples (total thickness ~6 mm) were sectioned into four symmetric parts. One section from each couple was metallographically examined to verify bonding quality.

Subsequently, the diffusion couples were sealed in evacuated quartz capsules (10^{-5} mbar) and annealed for 100 h at 800 °C (DC2), 24 h at 900 °C (DC2), and 72 h at 1000 °C (DC1). After annealing, the samples were water-quenched by breaking the quartz capsules under water. A second set of diffusion couples was annealed under flowing Ar–4%H_2 using identical time–temperature conditions to enable rapid quenching. No significant differences were observed between samples annealed in vacuum and in Ar–4%H_2.

2.4. Microstructural analyses

The annealed diffusion couples were sectioned and mounted in a conductive phenolic resin (Polyfast, Struers, Copenhagen, Denmark). Prior to mounting, oxidized specimens were coated with a 5 nm Au layer and subsequently electroplated with Ni to preserve the oxide scale.

The mounted samples were ground with SiC papers to a P4000 surface finish and polished to 0.25 μm with diamond pastes. Final surface preparation was performed by ion milling using a Hitachi ArBlade 5000 system.

Microstructural characterization and compositional analysis were carried out using a field-emission environmental scanning electron microscope (FEI Quanta 200 ESEM) equipped with an energy-dispersive X-ray spectroscopy (EDS) system.

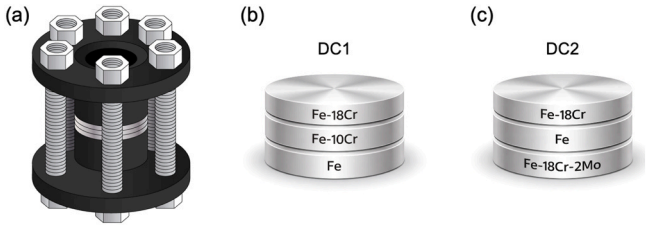

Fig. 1. Schematic illustration of (a) the clamping device used for diffusion welding of cylindrical specimens (21 mm outer diameter, 2 mm thickness), and the configurations of the diffusion couples: (b) Fe–18Cr / Fe–10Cr / Fe (DC1) and (c) Fe–18Cr / Fe / Fe–18Cr–2Mo (DC2).

2.5. Interdiffusion simulation

Interdiffusion simulations were performed using the DICTRA [40] software with the TCFE6 [41] thermodynamic and MOB2 [42] mobility databases. A double geometric grid was employed with geometric grid factors of 1.03 and 0.97. The computational domain was discretized using 100 grid nodes. The simulation domain width was 0.2 mm for the simulations at 800 °C (100 h) and 900 °C (24 h), and 2 mm for the simulation at 1000 °C (72 h). Stable BCC_A2 and FCC_A1 phases were included in the calculations. The initial time step was set to 1×10^{-7} s. The initial concentration profile was defined as a step function corresponding to the nominal alloy compositions, with the interface located at the center of the simulation domain.

3. Results

3.1. Oxidation at 900 °C – beneficial effect of Mo

Fig. 2 shows the oxygen uptake curves for Fe–18Cr and Fe–18Cr–2Mo exposed to Ar–4%H_2–7%H_2O at 900 °C for 72 h. Under these conditions, where FeO is thermodynamically stable, Fe–18Cr exhibited breakaway oxidation, with a mass gain of 26.2 mg/cm^2. In contrast, Fe–18Cr–2Mo showed significantly lower oxygen uptake (1.3 mg/cm^2), in good agreement with literature values for Fe–20Cr [43].

BSE SEM images (Fig. 3) reveal breakaway oxidation at the specimen edges in Fe–18Cr, whereas Fe–18Cr–2Mo exhibits protective behavior. High-magnification images (insets in Fig. 3) show external Cr_2O_3 scales forming in the specimen center. The chromia scales on both alloys have similar morphology and thickness (8.0 ± 0.3 μm), corresponding to the oxygen uptake of 1.32 mg/cm^2 assuming pure Cr_2O_3.

Chromium depletion profiles measured by EDX (Fig. 4) show similar interface Cr concentrations: 13.2 wt% for Fe–18Cr and 12.7 wt% for Fe–18Cr–2Mo. The profiles are well described by the classical Wagner model of selective oxidation [10], using experimentally determined parabolic rate constants and literature values of Cr diffusivity [33]. These results indicate that the addition of 2 wt% Mo does not significantly affect Cr diffusion in Fe–18Cr at 900 °C.

3.2. Interdiffusion

Fig. 5 shows a section of the Fe–Cr phase diagram highlighting the so-called γ-loop, i.e., the compositional region between 0 and ~14 wt% Cr in the temperature range 830–1375 °C. Within the γ-loop, Fe–Cr alloys exhibit an austenitic (γ) microstructure with a face-centered cubic (FCC) lattice, whereas outside this region they are ferritic (α) with a body-centered cubic (BCC) lattice.

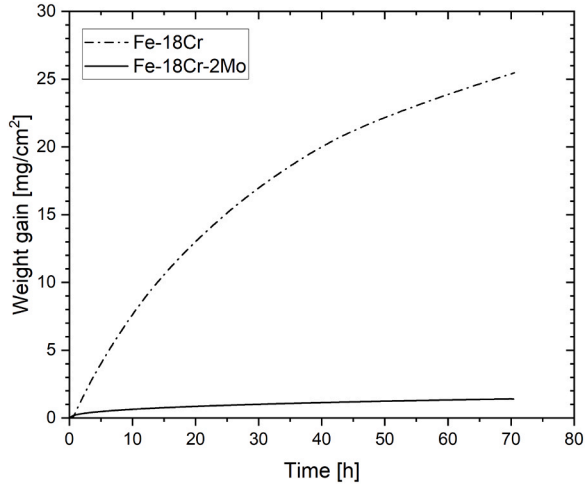

Fig. 2. Weight change curves for Fe–18Cr and Fe–18Cr−2Mo exposed for 72 h to Ar−4%H_2−7%H_2O at 900 °C in thermobalance.

The reference diffusion couple experiments were designed to study interdiffusion within single-phase regions, avoiding phase transformations. An austenitic diffusion couple (Fe−10Cr/Fe, A–B in Fig. 5) was investigated at 1000 °C, and a ferritic diffusion couple (Fe−18Cr/Fe, F–G in Fig. 5) at 800 °C.

Interdiffusion involving phase transformations was studied using diffusion couple Fe−18Cr/Fe (D–E in Fig. 5) at 900 °C and Fe−18Cr/Fe−10Cr (B–C in Fig. 5) at 1000 °C. At 900 °C, both end members of this couple (pure Fe and Fe–18Cr) are ferritic at 900 °C. However, the diffusion path intersects the γ-phase field, leading to the formation of an FCC (austenitic) region within the interdiffusion zone.

At 1000 °C, diffusion couple Fe−18Cr/Fe−10Cr (B–C in Fig. 5) intersects the γ-loop only once, forming a BCC layer that grows toward the Fe–10Cr side along the Cr concentration gradient.

3.2.1. Single-phase diffusion at 800 and 1000 °C

The BSE SEM image in Fig. 6**a** shows the interdiffusion zone in the Fe–18Cr / Fe diffusion couple after annealing for 100 h at 800 °C. Both end members, Fe–18Cr and pure Fe, are ferritic (BCC) at 800 °C (see Fig. 5); therefore, no phase transformation occurs in the interdiffusion zone. The Cr concentration profile (Fig. 6**b**) exhibits a classical Boltzmann error-function-type distribution. The experimental measurements are in very good agreement with the DICTRA simulation.

In contrast, the interdiffusion zone in the austenitic diffusion couple Fe–10Cr / Fe (see SEM image in Fig. 7**a**), annealed for 72 h at 1000 °C, differs from that of the ferritic diffusion couple at 800 °C (Fig. 6**a**). The Fe–10Cr side of the diffusion couple exhibits a fine-grained microstructure, resulting in a brighter BSE contrast compared to the Fe side. Both end members lie within the γ-loop and are therefore austenitic (FCC) at 1000 °C; however, they transform back to ferrite (BCC) upon cooling to room temperature. The Cr concentration profile in Fig. 7**b** follows an error-function-type distribution and agrees very well with the DICTRA simulation for the FCC phase. This indicates that the phase transformation in Fe–10Cr occurs during cooling.

3.2.2. Ferrite growth at 1000 °C

The interdiffusion zone at 1000 °C may differ if the diffusion path intersects the phase boundary of the γ-loop (Fe−18Cr/Fe−10Cr couple, B–C in Fig. 5). Fig. 8**a** shows a BSE SEM micrograph of the interdiffusion zone in the Fe–18Cr / Fe–10Cr diffusion couple. Similar to the Fe–10Cr / Fe diffusion couple (Fig. 7**a**), the Fe–10Cr side transforms into fine-grained ferrite upon cooling. The main feature of this ferrite–austenite diffusion couple is the formation of a new layer growing into the austenitic Fe–10Cr side. The thickness of this layer after 72 h at 1000 °C is 87 μm.

The Cr concentration profile (Fig. 8**b**) deviates from the classical homogenization distribution expected for single-phase diffusion. Instead, the Cr profile exhibits a step-function-like behavior, with a sharp drop in Cr concentration at the newly formed interface from 13.5 to 10 wt%. The measured Cr concentration profile is in very good agreement with the DICTRA simulation, which accurately predicts the position of the new interface. Furthermore, the simulated concentration profile closely resembles the experimentally measured profiles reported by Nishizawa and Chiba [34] for α/γ diffusion couples, providing additional validation of the present modeling approach.

3.2.3. Austenite formation at 900 °C

The most interesting diffusion couple in the context of this study is Fe–18Cr / Fe. Similar to 800 °C, both end members, Fe–18Cr and pure Fe, are ferritic (BCC) at 900 °C (couple D–E, Fig. 5). However, the diffusion path between 0 and 18 wt% Cr at 900 °C intersects the γ-loop twice. This implies that this diffusion couple can reproduce the chromium depletion that develops in Fe–18Cr during oxidation (Fig. 4), but

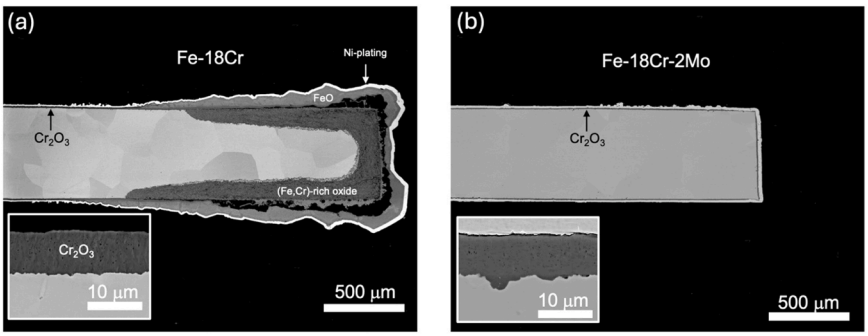

Fig. 3. BSE SEM images of cross-sectioned Fe–18Cr (a) and Fe–18Cr–2Mo (b) after 72 h exposure at 900 °C in Ar–4%H_2–7%H_2O (above the FeO equilibrium). The overview micrographs show the edges of the 0.6 mm thick specimens, whereas the high-magnification insets display the Cr_2O_3 scales formed at the specimen center.

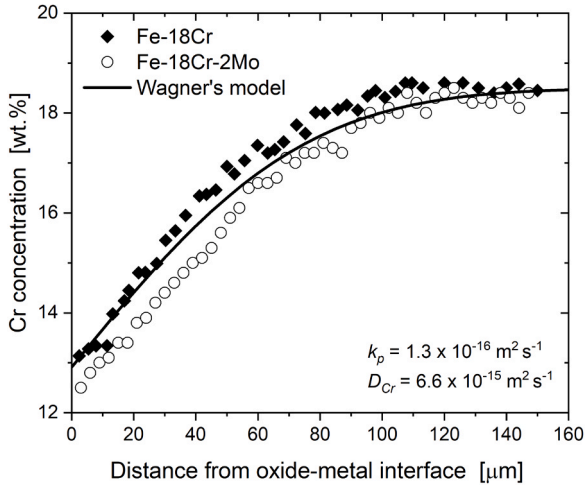

Fig. 4. Chromium depletion profiles beneath the external Cr_2O_3 scale in Fe–18Cr (full rhombs) and Fe–18Cr–2Mo (empty circles) after 72 h exposure in Ar–4%H_2–7%H_2O at 900 °C, as measured by EDS. The solid line represents the calculated Cr depletion profile using the classical Wagner model [18]. The parabolic rate constant was determined experimentally from the Cr_2O_3 scale thickness measured in the SEM images. The interdiffusion coefficient of Cr was taken from Ref. [18].

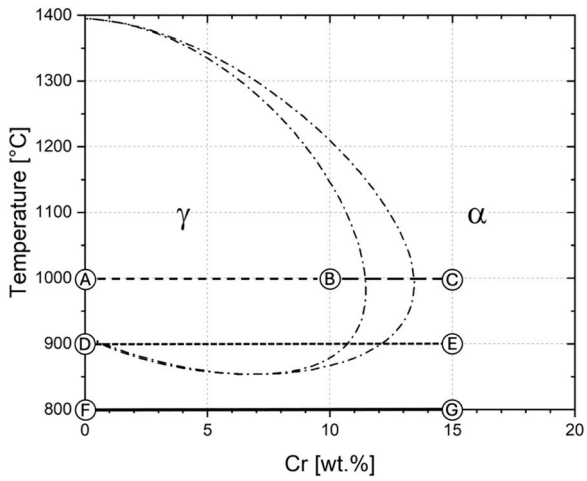

Fig. 5. Fragment of the binary Fe–Cr phase diagram showing the γ-loop, calculated using Thermo-Calc with the TCFE6 thermodynamic database. Points A–G represent the end-member compositions of the diffusion couples.

under oxidation-free conditions. This enables the isolated investigation of diffusion-induced phase transformations without the complicating effects of oxidation.

The BSE SEM micrograph in Fig. 9**a** shows a new phase formed between Fe–18Cr and Fe after annealing for 24 h at 900 °C. The layer thickness is 11 µm. Similar to the previous examples, the DICTRA simulation accurately predicts the Cr concentration profile (Fig. 9**b**) as well as the position of the new interface in the calculated spatial phase distribution (see Fig. 10). Interestingly, the present results also demonstrate small deviations of the experimentally measured Cr concentrations at the α/γ phase boundaries from the equilibrium values. Similar deviations were previously reported by Nishizawa and Chiba [34] for Fe–Cr α/γ diffusion couples, who interpreted these observations as evidence that the moving α/γ interface is not in local equilibrium, but instead exhibits a finite interfacial resistance to atomic transfer associated with limited interface mobility. The origin of these deviations from the equilibrium values remains unclear and is beyond the scope of the present study.

3.2.4. *Visualization of austenite and effect of Mo*

A new layer in the Fe–18Cr / Fe diffusion couple (Fig. 9**a** and Fig. 10**b**) forms as a result of austenitization. This will be discussed in more detail in the following section. EBSD analysis (not shown here) revealed that the entire diffusion couple is ferritic (BCC), indicating that the austenite transforms back to ferrite upon cooling. Presumably, the compositions of the austenite at the boundaries of the newly formed layer are very close to the corresponding α/γ phase boundaries (see Fig. 5 and Fig. 9**b**), enabling rapid transformation to BCC, unlike in the Fe–10Cr case at 1000 °C. Thus, compositions further away from the boundaries of the γ-loop are required to clearly visualize austenitization in this diffusion couple.

This can be achieved by a two-step annealing treatment. First, the Fe–18Cr / Fe diffusion couple is annealed for 100 h at 800 °C, resulting in a homogeneous Cr distribution across the diffusion couple, as demonstrated in Fig. 6. In the second step, the temperature is immediately increased from 800 to 900 °C, and the diffusion couple is water-quenched after 1 h at 900 °C.

Fig. 11**a** shows a BSE SEM image of the interdiffusion zone in the Fe–18Cr / Fe diffusion couple after two-step annealing. The entire interdiffusion zone consists of fine, needle-like grains, indicating rapid transformation from FCC to BCC upon cooling. Interestingly, the addition of 2 wt% Mo (Fig. 11**b**) completely suppresses this transformation, indicating that the Fe–18Cr–2Mo / Fe diffusion couple remains fully ferritic (BCC) across the entire interdiffusion zone. In addition to the thermodynamic stabilization of ferrite, partitioning of Mo at the migrating α/γ interface may reduce interface mobility through a solute-drag effect [44,45]. The present experiments do not permit a quantitative assessment of this mechanism, and its contribution remains to be clarified in future studies.

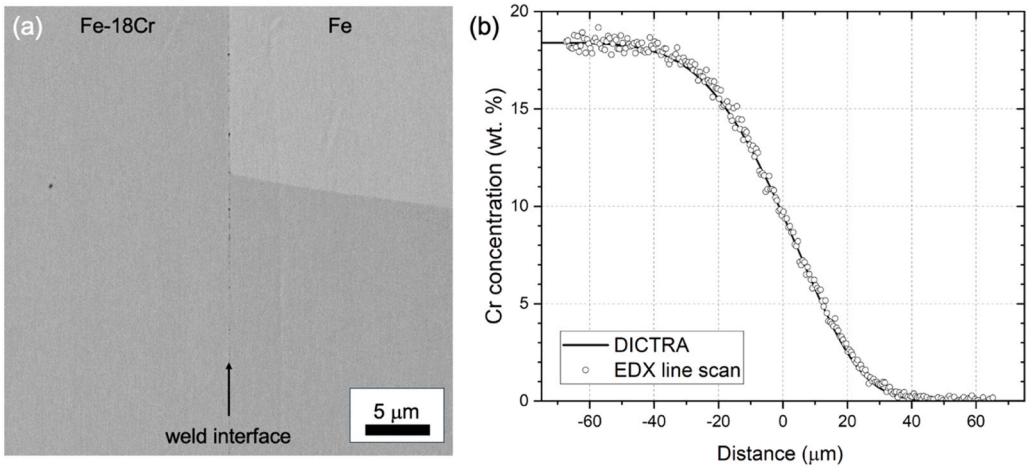

Fig. 6. (a) BSE SEM micrograph of the interdiffusion zone in the ferritic Fe–18Cr / Fe diffusion couple (F–G, see Fig. 5) after 100 h at 800 °C. (b) Cr concentration profile measured with EDX and compared with a DICTRA simulation.

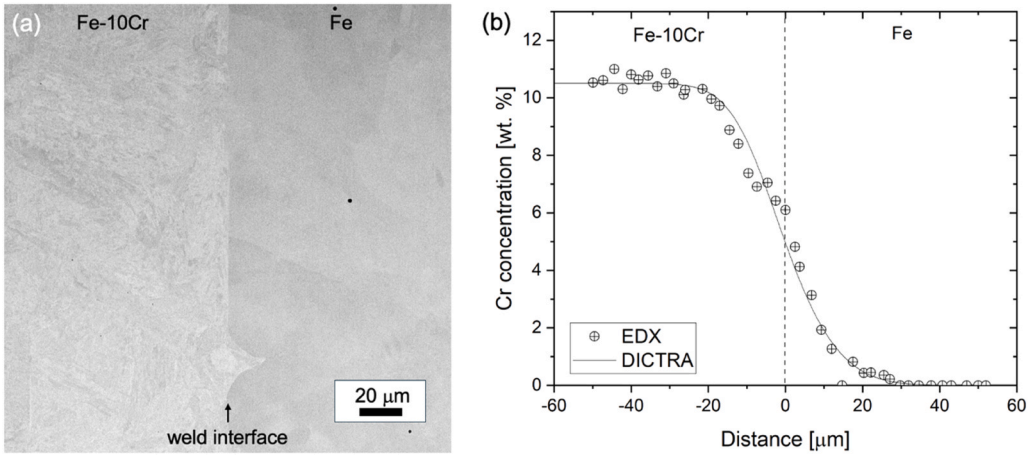

Fig. 7. (a) BSE SEM micrograph of the interdiffusion zone in the austenitic Fe–10Cr / Fe diffusion couple (A–B, see Fig. 5) after 72 h at 1000 °C. (b) Cr concentration profile measured with EDX and compared with a DICTRA simulation.

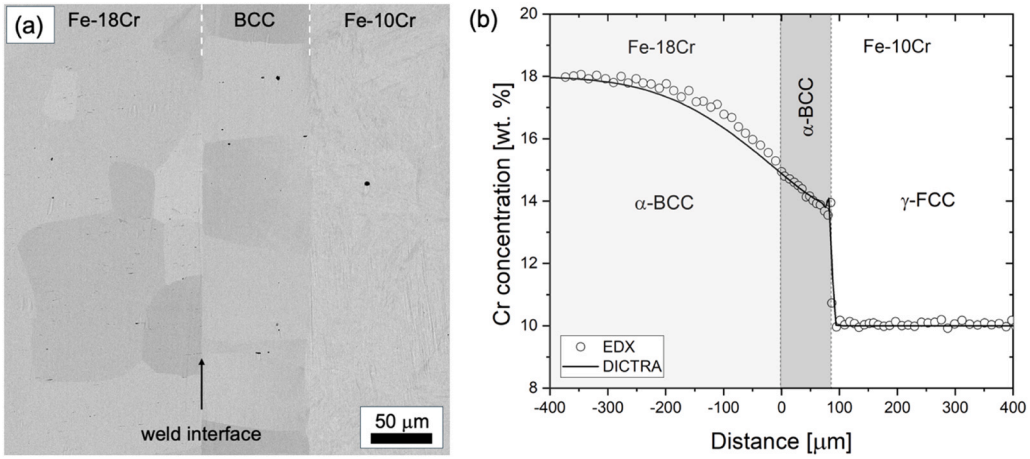

Fig. 8. (a) BSE SEM micrograph of the interdiffusion zone in the Fe–18Cr / Fe–10Cr diffusion couple (B–C, see Fig. 5) after 72 h at 1000 °C. (b) Cr concentration profile measured with EDX and compared with DICTRA-simulated Cr profile. White dashed lines indicate a newly formed layer in the interdiffusion zone.

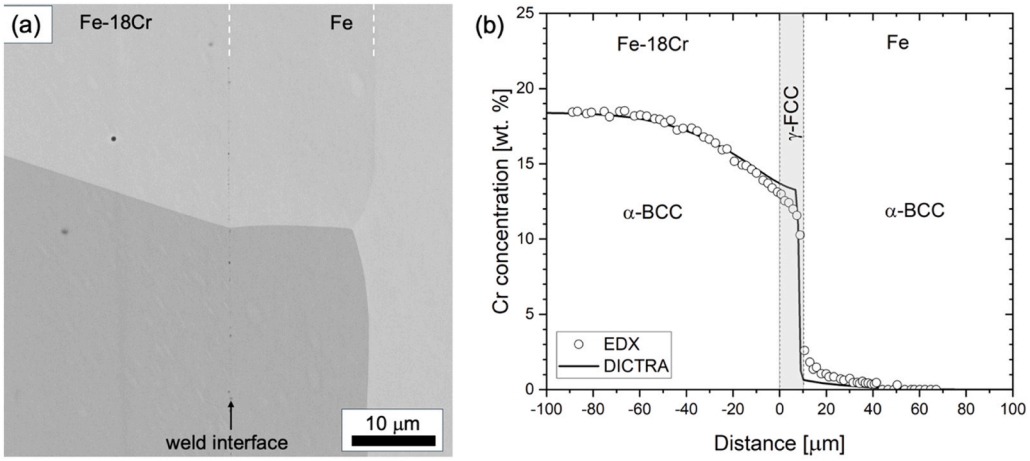

Fig. 9. (a) BSE SEM micrograph of the interdiffusion zone in the Fe–18Cr / Fe diffusion couple (D–E, see Fig. 5) after 24 h at 900 °C. (b) Cr concentration profile measured with EDX and compared with DICTRA-simulated Cr profile. White dashed lines indicate a newly formed layer in the interdiffusion zone.

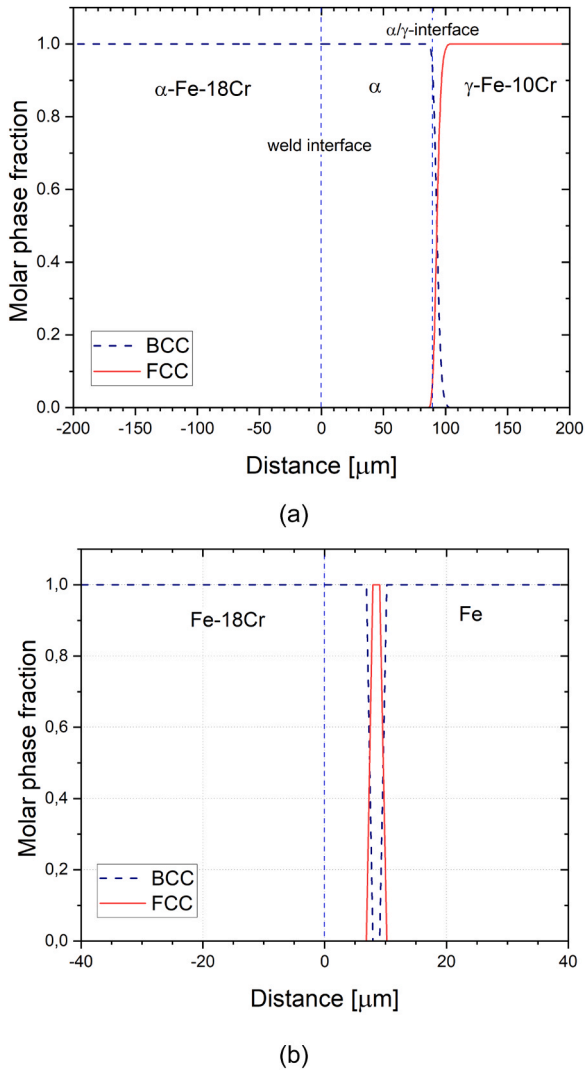

Fig. 10. DICTRA simulations of a new phase formation in diffusion couples (a) Fe–18Cr / Fe–10Cr (B–C in Fig. 5) after 72 h at 1000 °C, and (b) Fe–18Cr / Fe (D–E in Fig. 5) after 24 h at 900 °C. Simulations were performed using the TCFE6 [41] and MOB2 [42] databases.

4. Discussion

4.1. Oxidation and austenitization

The addition of only 2 wt% Mo to Fe–18Cr leads to a dramatic improvement in oxidation resistance (Fig. 2 and Fig. 3). This pronounced effect is not readily explained by classical concepts of selective oxidation theory introduced by Wagner [10], since Mo has a negligible influence on the key transport properties governing oxidation. Both Fe–18Cr and Fe–18Cr–2Mo form Cr_2O_3 scales of comparable thickness (Fig. 3), indicating similar oxidation kinetics and, consequently, comparable chromium consumption rates. Consistently, the subsurface Cr depletion profiles (Fig. 4) are only marginally affected by the addition of Mo.

These observations indicate that the role of Mo is primarily thermodynamic rather than kinetic. Fig. 12 shows a calculated section of the Fe–Cr–Mo system, comparing the γ-loop in the binary Fe–Cr system with that in the presence of 2 wt% Mo. As a ferrite stabilizer [46], Mo significantly contracts the γ-loop, so that at 900 °C the entire compositional range remains ferritic in Fe–18Cr–2Mo. In contrast, the binary Fe–18Cr alloy undergoes an α-to-γ transformation upon Cr depletion to approximately 12.7 wt%, which closely corresponds to the experimentally measured Cr concentration at the oxide-metal interface (Fig. 4).

During oxidation, Cr depletion is spatially non-uniform in rectangular specimens. It is enhanced at specimen edges and corners due to geometrical effects [47,48]. As a result, local compositions at these locations can enter the γ-phase field, promoting austenite formation. Notably, these regions coincide with the sites where breakaway oxidation is initiated (Fig. 3), suggesting a direct link between austenitization and the onset of non-protective breakaway oxidation.

The hypothesis that austenite formation triggers breakaway oxidation in Fe–Cr alloys has been discussed in literature since the late 1960s; however, direct experimental evidence has remained elusive. This is primarily due to two factors. First, the newly formed austenite is highly susceptible to rapid internal oxidation [25], leading to its immediate consumption. Since the diffusivity of Cr in FCC is approximately two orders of magnitude lower than in BCC (Table 1), chromium transport to the oxide-alloy interface becomes severely restricted. As a result, the alloy surface becomes critically depleted in chromium and can no longer sustain the growth of a protective Cr_2O_3 scale, resulting in rapid internal oxidation followed by the formation of Fe-rich oxides. Second, any remaining austenite transforms back to ferrite upon cooling, rendering post-mortem detection difficult.

Previous studies have therefore relied primarily on indirect evidence. Alloying Fe–Cr model alloys with 2–5 wt% Mo has been shown to

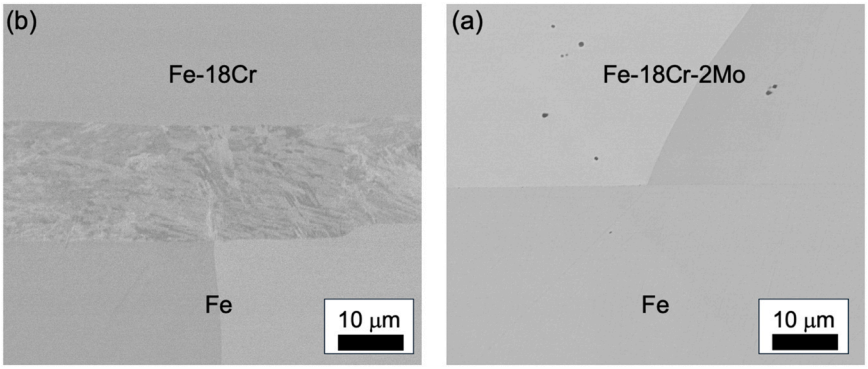

Fig. 11. BSE SEM micrographs of the interdiffusion zone in (a) Fe–18Cr / Fe and (b) Fe–18Cr–2Mo / Fe diffusion couples after two-step annealing: 100 h at 800 °C immediately followed by 1 h at 900 °C.

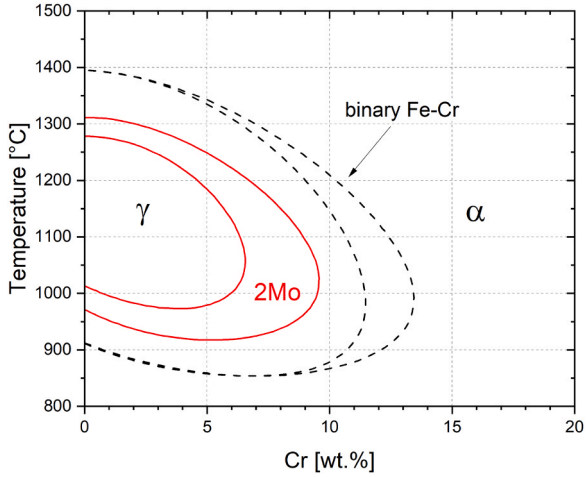

Fig. 12. Fragment of the binary Fe–Cr phase diagram illustrating the effect of alloying Fe–Cr with 2 wt% Mo on the γ-loop (black dashed lines), calculated using Thermo-Calc with the TCFE9 database.

suppress breakaway oxidation and promote the formation of protective Cr_2O_3 scales [24], consistent with the stabilization of the BCC phase [46]. In commercial ferritic stainless steels (e.g., Crofer 22 APU), austenitization-affected zones (AAZs) have been identified after prolonged oxidation, exhibiting fine-grained ferritic microstructures indicative of prior γ-phase formation [49]. More recently, in-situ high-temperature XRD experiments [50] have directly demonstrated transient α-to-γ transformations in Cr-depleted powder particles of Crofer 22 APU during oxidation, followed by rapid formation of Fe-rich oxides.

In this context, the present results (Fig. 9 and Fig. 11) provide direct experimental evidence of austenite formation in binary Fe–Cr alloys under well-controlled, oxidation-free conditions. The needle-like microstructure observed after quenching (Fig. 11**a**) is characteristic of rapid γ-to-α transformation and closely resembles the reported AAZ microstructures [49,50], supporting the interpretation that austenite forms in the Fe–18Cr / Fe diffusion couple during annealing at 900 °C. Importantly, the diffusion couple approach enables the isolation of diffusion-driven phase transformations from concurrent oxidation processes, thereby overcoming the limitations of the oxidation experiments.

Finally, the measured thickness of the newly formed layer (Fig. 9**a**) provides a quantitative measure for estimating the interdiffusion coefficient in this phase, offering an additional means of phase identification and validation of the transformation pathway.

4.2. Modeling interdiffusion and phase transformations

The interdiffusion behavior in the Fe–Cr system can be rationalized using both classical analytical approaches [51] and CALPHAD-based numerical simulations, e.g., DICTRA [40]. The single-phase calculations (Fig. 6 and Fig. 7) serve primarily to validate the experimental conditions as they reproduce the expected error-type concentration profiles.

The analytical descriptions of phase growth in diffusion systems originate from the classical work of Carl Wagner [52], who developed a model for solid-state reactions such as oxidation, sulfidation, and halogenation. The approach introduced the parabolic rate constant, k_p, a key parameter relating the thickness of a growing phase to time:

$$X^2 = 2k_p t \quad (1)$$

where X is the thickness of the product layer (m), t is time (s), and k_p is the parabolic rate constant ($m^2\ s^{-1}$).

Wagner expressed k_p as the integral over the chemical potential gradient across the growing phase. For oxide scales, this can be written in terms of the oxygen partial pressure:

Table 1
Interdiffusion coefficients, $\tilde{D}_{Fe-Cr}$, for BCC and FCC phases, determined from interdiffusion profiles using the Boltzmann solution for single-phase diffusion and from experimentally measured phase growth kinetics in diffusion couples intersecting the γ-loop via Eq. (3). The obtained values are compared with literature data [33].

Diffusion couple	phase	T [°C]	t [h]	X [µm]	k_p [m^2s^{-1}]	$\tilde{D}_{Fe-Cr}$ [m^2s^{-1}] Experiment	$\tilde{D}_{Fe-Cr}$ [m^2s^{-1}] Literature
no phase formation							
Fe–18Cr / Fe	BCC	800	100	-	-	$(6.62 \pm 0.24) \times 10^{-16}$	9.0×10^{-16}
Fe–10Cr / Fe	FCC	1000	72	-	-	$(2.3 \pm 0.2) \times 10^{-16}$	2.8×10^{-16}
phase formation							
Fe–18Cr / Fe	FCC	900	24	11.2 ± 0.4	$(7.3 \pm 0.5) \times 10^{-16}$	$(1.24 \pm 0.05) \times 10^{-17}$	3.6×10^{-17}
Fe–18Cr / Fe–10Cr	BCC	1000	72	87 ± 0.9	$(1.46 \pm 0.03) \times 10^{-14}$	$(1.44 \pm 0.04) \times 10^{-14}$	1.4×10^{-14}

$$k_p = \int_{p_{O_2}^{M/O}}^{p_{O_2}^{G/O}} \widetilde{D}\, d\ln p_{O_2} \quad (2)$$

where $p_{O_2}^{M/O}$ and $p_{O_2}^{G/O}$ denote the oxygen partial pressures at metal-oxide and gas-oxide interfaces, respectively, and $\widetilde{D}$ is the effective interdiffusion coefficient, incorporating both defect transport and thermodynamic driving force [52].

This formalism was later extended by Wagner [53] to multiphase binary diffusion couples, enabling the determination of the interdiffusion coefficients in the newly formed phases directly from measurable quantities such as layer thickness.

For a diffusion couple forming a new phase (e.g. Fig. 8 and Fig. 9), the interdiffusion coefficient of the growing phase can be expressed as:

$$\widetilde{D} = \frac{1}{2t}\left(\frac{dN_{Cr}}{dx}\right)^{-1}\left[(1-Y)\int_{-\infty}^{x} Y dx + Y\int_{x}^{+\infty}(1-Y)dx\right] \quad (3)$$

where x is the space coordinate (m), N_{Cr} is mole fraction of Cr, and Y is the normalized composition variable [54] defined as

$$Y = \frac{N_{Cr} - N_{Cr}^{-\infty}}{N_{Cr}^{+\infty} - N_{Cr}^{-\infty}} \quad (4)$$

Here, $N_{Cr}^{-\infty}$ and $N_{Cr}^{+\infty}$ represent the compositions of the end members of the diffusion couple in terms of mole fraction.

Eq. (3) was applied to determine the interdiffusion coefficient in the BCC phase at 1000 °C (Fig. 8) and the FCC phase at 900 °C (Fig. 9), using experimentally measured layer thickness (see Table 1), annealing times, and concentration gradients from EDX profiles. The calculated values of $\widetilde{D}_{Fe-Cr}$ are in excellent agreement with the literature data [33], yielding $(1.44 \pm 0.04) \times 10^{-14}$ m^2s^{-1} for BCC at 1000 °C and $(1.24 \pm 0.05) \times 10^{-17}$ m^2s^{-1} for FCC at 900 °C.

At 1000 °C, $\widetilde{D}_{Fe-Cr}$ is very close to the parabolic rate constant k_p, which can be attributed to the relatively shallow concentration gradient across the BCC layer (Fig. 8), in contrast to the steeper Cr concentration gradient observed in the FCC layer at 900 °C (Fig. 9).

The successful application of Wagner's approach has two important implications. First, the calculated value of $\widetilde{D}_{Fe-Cr}$ for the layer formed at 900 °C provides indirect confirmation that the growing phase is austenitic, even though it transforms to ferrite upon cooling and cannot be directly identified *post-mortem*. Second, the excellent agreement between experimental results and DICTRA simulations demonstrates that the homogenization model [55] implemented in DICTRA as well as the thermodynamic and mobility databases reliably predict both phase growth kinetics (interface positions, Fig. 10) and concentration profiles in multiphase Fe–Cr diffusion systems (Fig. 8**b** and Fig. 9**b**).

4.3. Martensite or Widmanstätten ferrite in Fe–10Cr?

An important observation requiring further discussion is the characteristic needle-like microstructure formed in Fe–10Cr diffusion couples after quenching from 1000 °C (Fig. 7**a** and Fig. 8**a**). Similar morphologies have been reported for Fe–10Cr alloys quenched from 1050 °C and were identified as Widmanstätten ferrite. Bee and Honeycombe [56] demonstrated that, in low-carbon Fe–10Cr alloys, the decomposition of austenite above 600 °C produces equiaxed and Widmanstätten ferrite, whereas martensitic transformation occurs only below 500 °C.

Comparable needle-like microstructures have also been observed in austenitization-affected zones (AAZs) formed in thin foils of commercial ferritic stainless steel Crofer 22 APU (Fe–23Cr) after prolonged oxidation [49,50]. Such features can be easily misinterpreted as martensite, since martensitic transformation is commonly expected upon cooling of steels with compositions within or near the γ-loop (Fig. 5). However, the formation of martensite requires both sufficient carbon content and high cooling rates. In the present model alloys, the carbon content is extremely low, and the cooling rates during quenching are relatively moderate. For comparison, martensitic microstructures in iron-based alloys typically require significantly higher carbon contents and rapid cooling rates (e.g., 30–300 K s^{-1} in commercially pure iron containing >0.03 wt% C) [35].

The brighter contrast observed in BSE SEM images of the AAZ is often attributed to a high density of defects and lattice distortions associated with fine, highly misoriented grains [57]. However, such contrast alone is insufficient to identify martensite. Color etching of the quenched diffusion couples using Kalling's reagent ($CuCl_2$ + HCl) revealed no characteristic martensitic features [11]. Furthermore, EBSD and TEM/SAED analyses reported in Refs. [49,50] confirm that the needle-like grains in the AAZ are ferritic (BCC).

It is therefore concluded that the FCC phase present in Fe–10Cr at 1000 °C transforms predominantly into Widmanstätten ferrite during cooling. In contrast, the thin FCC layer formed in the Fe–18Cr / Fe diffusion couple at 900 °C (Fig. 9**a** and Fig. 10**b**) transforms rapidly back to BCC ferrite upon quenching, consistent with its composition being close to the α/γ phase boundaries.

5. Conclusions

This work provides direct experimental and computational evidence of diffusion-induced phase transformations across the α/γ boundary in Fe–Cr alloys above 830 °C and clarifies their implications for high-temperature oxidation behavior:

- Diffusion-induced phase transformations in Fe–Cr diffusion couples occur when the diffusion path intersects the γ-loop, temperature and composition.
- DICTRA simulations accurately reproduce concentration profiles, phase distributions, and interface positions, demonstrating the predictive capability of CALPHAD-based thermodynamic and kinetic descriptions of the Fe–Cr system.
- Wagner's classical analysis yielded interdiffusion coefficients of $(1.24 \pm 0.05) \times 10^{-17}$ m^2s^{-1} for the FCC phase at 900 °C and $(1.44 \pm 0.04) \times 10^{-14}$ m^2s^{-1} for the BCC phase at 1000 °C, in excellent agreement with literature values and DICTRA simulations.
- Austenite formation in Fe–Cr alloys during high-temperature oxidation is driven by chromium depletion under diffusion-controlled conditions, as independently demonstrated in oxidation-free diffusion couples.
- Alloying with Mo (and potentially other ferrite stabilizers) suppresses austenitization by stabilizing ferrite (BCC), preventing the formation of FCC at 900 °C and thereby inhibiting breakaway oxidation.

CRediT authorship contribution statement

Anton Chyrkin: Writing – review & editing, Writing – original draft, Visualization, Validation, Resources, Project administration, Methodology, Investigation, Funding acquisition, Formal analysis, Data curation, Conceptualization.

Declaration of Competing Interest

The author declares that he has no known competing financial interests or personal relationships that could have appeared to influence the work reported in this paper.

Acknowledgements

This work was funded by the European Union, project MSCA4Ukraine, grant No. 1232975. The present publication reflects only the

author's views, and the European Union is not liable for any use that may be made of the information contained therein. Dr. D. Naumenko and Mr. H. Cosler from Forschungszentrum Jülich GmbH are acknowledged for the thermobalance experiments. Dr. D. Naumenko is kindly acknowledged for reading and commenting on the manuscript.

References

[1] J.R. Davis, ASM Specialty Handbook: Stainless Steels, ASM International, Almere, Netherlands, 1994.
[2] P. Spätig, J.C. Chen, G.Robert Odette, Ferritic and tempered martensitic steels, Struct. Alloy. Nucl. Energy Appl. (2019) 485–527, https://doi.org/10.1016/B978-0-12-397046-6.00011-3.
[3] K. Chen, S.P. Jiang, Review—Materials degradation of solid oxide electrolysis cells, J. Electrochem. Soc. 163 (2016) F3070–F3083, https://doi.org/10.1149/2.0101611jes.
[4] W.J. Quadakkers, J. Piron-Abellan, V. Shemet, L. Singheiser, Metallic interconnectors for solid oxide fuel cells–a review, Mater. High. Temp. 20 (2003) 115–127, https://doi.org/10.3184/096034003782749071.
[5] A. Hauch, R. Küngas, P. Blennow, A.B. Hansen, J.B. Hansen, B.V. Mathiesen, M. B. Mogensen, Recent advances in solid oxide cell technology for electrolysis, Science (1979) 370 (2020), https://doi.org/10.1126/science.aba6118.
[6] Y. Xu, S. Cai, B. Chi, Z. Tu, Technological limitations and recent developments in a solid oxide electrolyzer cell: A review, Int. J. Hydrog. Energy 50 (2024) 548–591, https://doi.org/10.1016/J.IJHYDENE.2023.08.314.
[7] P. Huczkowski, A. Chyrkin, L. Singheiser, W. Nowak, W.J. Quadakkers, Corrosion behavior of candidate heat exchanger materials in oxidizing and reducing gases, relevant to oxyfuel combustion, 2016.
[8] L. Faivre, P.O. Santacreu, A. Acher, A new ferritic stainless steel with improved thermo-mechanical fatigue resistance for exhaust parts, Mater. High. Temp. 30 (2013) 36–42, https://doi.org/10.3184/096034013X13637176323444.
[9] C. Wagner, Theoretical Analysis of the diffusion processes determining the oxidation rate of alloys, J. Electrochem. Soc. 99 (1952) 369, https://doi.org/10.1149/1.2779605.
[10] C. Wagner, Oxidation of alloys involving noble metals, J. Electrochem. Soc. 103 (1956) 571, https://doi.org/10.1149/1.2430159.
[11] J. Ehlers, D.J. Young, E.J. Smaardijk, A.K. Tyagi, H.J. Penkalla, L. Singheiser, W. J. Quadakkers, Enhanced oxidation of the 9%Cr steel P91 in water vapour containing environments, Corros. Sci. 48 (2006) 3428–3454, https://doi.org/10.1016/j.corsci.2006.02.002.
[12] B. Pujilaksono, T. Jonsson, H. Heidari, M. Halvarsson, J.-E. Svensson, L.-G. Johansson, Oxidation of Binary FeCr Alloys (Fe–2.25Cr, Fe–10Cr, Fe–18Cr and Fe–25Cr) in O2 and in O2 + H2O environment at 600 °C, Oxid. Met. 75 (2011) 183–207, https://doi.org/10.1007/s11085-010-9229-z.
[13] H. Asteman, J.E. Svensson, L.G. Johansson, Evidence for chromium evaporation influencing the oxidation of 304L: The effect of temperature and flow rate, Oxid. Met. 57 (2002) 193–216, https://doi.org/10.1023/A:1014877600235.
[14] G.R. Holcomb, Calculation of reactive-evaporation rates of chromia, Oxid. Met. 69 (2008) 163–180, https://doi.org/10.1007/s11085-008-9091-4.
[15] D.J. Young, B.A. Pint, Chromium volatilization rates from Cr2O3 scales into flowing gases containing water vapor, Oxid. Met. 66 (2006) 137–153, https://doi.org/10.1007/s11085-006-9030-1.
[16] T. Norby, Protonic defects in oxides and their possible role in high temperature oxidation, Le. J. De. Phys. IV 03 (C9) (1993) 99–C9-106, https://doi.org/10.1051/jp4:1993907.
[17] B. Tveten, G. Hultquist, T. Norby, Hydrogen in chromium: Influence on the high-temperature oxidation kinetics in O2, oxide-growth mechanisms, and scale adherence, Oxid. Met. 51 (1999) 221–233, https://doi.org/10.1023/a:1018866505708.
[18] E. Essuman, G.H. Meier, J. Zurek, M. Hänsel, W.J. Quadakkers, The effect of water vapor on selective oxidation of Fe-Cr alloys, Oxid. Met. 69 (2008) 143–162, https://doi.org/10.1007/s11085-007-9090-x.
[19] E. Essuman, G.H. Meier, J. Zurek, M. Hänsel, L. Singheiser, W.J. Quadakkers, Enhanced internal oxidation as reason for breakdown of protective chromia scales on FeCr-alloys in water vapour containing gases, Pts 1 and 2 595–598, High. Temp. Corros. Prot. Mater. 7 (2008) 699–706.
[20] E. Essuman, G.H. Meier, J. Zurek, M. Hänsel, L. Singheiser, W.J. Quadakkers, Enhanced internal oxidation as trigger for breakaway oxidation of Fe-Cr alloys in gases containing water vapor, Scr. Mater. 57 (2007) 845–848, https://doi.org/10.1016/j.scriptamat.2007.06.058.
[21] D.P. Whittle, G.C. Wood, D.J. Evans, D.B. Scully, Concentration profiles in the underlying alloy during the oxidation of iron-chromium alloys, Acta Metall. 15 (1967) 1747–1755, https://doi.org/10.1016/0001-6160(67)90066-1.
[22] J. Zurek, G.H. Meier, E. Wessel, L. Singheiser, W.J. Quadakkers, Temperature and gas composition dependence of internal oxidation kinetics of an Fe-10%Cr alloy in water vapour containing environments, Mater. Corros. 62 (2011) 504–513, https://doi.org/10.1002/maco.201005865.
[23] D.J. Young, J. Zurek, L. Singheiser, W.J. Quadakkers, Temperature dependence of oxide scale formation on high-Cr ferritic steels in Ar-H2-H2O, Corros. Sci. 53 (2011) 2131–2141, https://doi.org/10.1016/j.corsci.2011.02.031.
[24] A. Chyrkin, J. Froitzheim, J. Zurek, D. Naumenko, Austenitization triggering breakaway oxidation of FeCr-base alloys at 900 °C, Corros. Sci. 244 (2025) 112605, https://doi.org/10.1016/J.CORSCI.2024.112605.
[25] A. Chyrkin, J. Froitzheim, W.J. Quadakkers, Transition from Internal to External Oxidation in Binary Fe–Cr Alloys Around 900 °C, High. Temp. Corros. Mater. 102 (2025) 1–22, https://doi.org/10.1007/S11085-024-10322-2/TABLES/5.
[26] A. Chyrkin, W.J. Quadakkers, Effect of α-to-γ transformation on internal oxidation in FeCr-base alloys in dry and wet gases, J. Alloy. Compd. 1045 (2025) 184722, https://doi.org/10.1016/J.JALLCOM.2025.184722.
[27] O.K. von Goldbeck, Iron-Chromium Fe-Cr, IRON - Bin. Phase Diagr. (1982) 31–34, https://doi.org/10.1007/978-3-662-08024-5_17.
[28] A. Jacob, E. Povoden-Karadeniz, E. Kozeschnik, Revised thermodynamic description of the Fe-Cr system based on an improved sublattice model of the σ phase, Calphad 60 (2018) 16–28, https://doi.org/10.1016/J.CALPHAD.2017.10.002.
[29] A.W. Bowen, G.M. Leak, Solute diffusion in alpha- and gamma-iron, 6 1, Metall. Trans. 1970 1 (1970) 1695–1700, https://doi.org/10.1007/BF02642019.
[30] R. Braun, M. Feller-Kniepmeier, Diffusion of chromium in α-iron, Phys. Status Solidi (a) 90 (1985) 553–561, https://doi.org/10.1002/PSSA.2210900219.
[31] C.G. Lee, Y. Iijima, K.I. Hirano, T. Hiratani, Diffusion of chromium in α-iron, Mater. Trans. JIM 31 (1990) 255–261, https://doi.org/10.2320/MATERTRANS1989.31.255.
[32] P.J. Alberry, C.W. Haworth, Interdiffusion of Cr, Mo, and W in Iron, Metal. Sci. 8 (1974) 407–412, https://doi.org/10.1179/msc.1974.8.1.407.
[33] P.I. Williams, R.G. Faulkner, Chemical volume diffusion coefficients for stainless steel corrosion studies, J. Mater. Sci. 22 (1987) 3537–3542, https://doi.org/10.1007/BF01161455/METRICS.
[34] T. Nishizawa, A. Chiba, Phenomenological Consideration on the Compositional Deviation from Equilibrium at the bcc/fcc Interface in Fe: Cr Diffusion Couples, Trans. Jpn. Inst. Met. 16 (1975) 767–778, https://doi.org/10.2320/MATERTRANS1960.16.767.
[35] D.J. YoungHigh Temperature Oxidation and Corrosion of Metals, High Temperature Oxidation and Corrosion of Metals: Second Edition, 2016 pp.1–733. https://doi.org/10.1016/C2014-0-00259-6..
[36] I. Barin, F. Sauert, E. Schultze-Rhonhof, W.S. Sheng, Thermochemical Data of Pure Substances, Part 1, Ag-Kr, VCH, 1993. https://books.google.com.ua/books?id=ekVGAAAAYAAJ.
[37] I. Barin, Thermochemical Data of Pure Substances, Wiley, 1995, https://doi.org/10.1002/9783527619825.
[38] M.H.Bin Ani, T. Kodama, M. Ueda, K. Kawamura, T. Maruyama, The effect of water vapor on high temperature oxidation of Fe-Cr alloys at 1073 K, Mater. Trans. 50 (2009) 2656–2663, https://doi.org/10.2320/matertrans.M2009212.
[39] A.R. Setiawan, M. Hanafi Bin Ani, M. Ueda, K. Kawamura, T. Maruyama, Oxygen permeability through internal oxidation zone in Fe-Cr alloys under dry and humid conditions at 973 and 1073 K, ISIJ Int. 50 (2010) 259–263, https://doi.org/10.2355/isijinternational.50.259.
[40] A. Borgenstam, A. Engström, L. Höglund, J. Ågren, DICTRA, a tool for simulation of diffusional transformations in alloys, J. Phase Equilibria 21 (2000) 269–280, https://doi.org/10.1361/105497100770340057/METRICS.
[41] Thermo-Calc, TCFE6 - TCS Steels/Fe-Alloys Database, Version 6.2, (2013).
[42] Thermo-Calc, MOB2 - TCS Alloys Mobility Database, version 2.7, (2009).
[43] L. Mikkelsen, S. Linderoth, High temperature oxidation of Fe–Cr alloy in O2–H2–H2O atmospheres; microstructure and kinetics, Materials Science Engineering A 361 (2003) 198–212, https://doi.org/10.1016/S0921-5093(03)00527-6.
[44] E.A. Antillon, C.A. Hareland, P.W. Voorhees, Solute trapping and solute drag during non-equilibrium solidification of Fe–Cr alloys, Acta Mater. 248 (2023) 118769, https://doi.org/10.1016/J.ACTAMAT.2023.118769.
[45] G. Miyamoto, K. Yokoyama, T. Furuhara, Quantitative analysis of Mo solute drag effect on ferrite and bainite transformations in Fe-0.4C-0.5Mo alloy, Acta Mater. 177 (2019) 187–197, https://doi.org/10.1016/J.ACTAMAT.2019.07.040.
[46] W. Gordon, A. Van Bennekom, Review of stabilisation of ferritic stainless steels, Mater. Sci. Technol. 12 (1996) 126–131, https://doi.org/10.1179/MST.1996.12.2.126.
[47] W.J. Quadakkers, D. Naumenko, S. Weinbruch, I. Gurrappa, Factors governing breakaway oxidation of FeCrAl-based alloys, Mater. Corros. 51 (2002) 224–235, https://doi.org/10.1002/(SICI)1521-4176(200004)51:4.
[48] W.M. Pragnell, H.E. Evans, Chromium depletion at 2-dimensional features during the selective oxidation of a 20Cr-25Ni austenitic steel, Oxid. Met. 66 (2006) 209–230, https://doi.org/10.1007/S11085-006-9039-5/FIGURES/13.
[49] A. Chyrkin, J. Froitzheim, Premature breakaway oxidation of ferritic stainless steels triggered by austenitization, Corros. Sci. 256 (2025) 113260, https://doi.org/10.1016/J.CORSCI.2025.113260.
[50] A. Chyrkin, D. Naumenko, M. Ziegner, E. Wessel, M. Sattari, J. Froitzheim, Effect of thermal cycling and phase transformations on chemical life of ferritic stainless steels, Corros. Sci. 264 (2026) 113779, https://doi.org/10.1016/J.CORSCI.2026.113779.
[51] H. Mehrer, Diffusion in Solids: Fundamentals. Methods, Materials, Diffusion-Controlled Processes, Springer-Verlag, Berlin Heidelberg, 2007.
[52] C. Wagner, Beitrag zur Theorie des Anlaufvorgangs, Z. F. üR. Phys. Chem. 21B (1933) 25–41, https://doi.org/10.1515/ZPCH-1933-2105.
[53] C. Wagner, The evaluation of data obtained with diffusion couples of binary single-phase and multiphase systems, Acta Metall. 17 (1969) 99–107, https://doi.org/10.1016/0001-6160(69)90131-X.
[54] F.J.A. den Broeder, A general simplification and improvement of the matano-boltzmann method in the determination of the interdiffusion coefficients in binary systems, Scr. Metall. 3 (1969) 321–325, https://doi.org/10.1016/0036-9748(69)90296-8.

[55] H. Larsson, A. Engström, A homogenization approach to diffusion simulations applied to α + γ Fe–Cr–Ni diffusion couples, Acta Mater. 54 (2006) 2431–2439, https://doi.org/10.1016/J.ACTAMAT.2006.01.020.
[56] J.V. Bee, R.W.K. Honeycombe, The isothermal decomposition of austenite in a high purity Iron-Chromium binary alloy, 9 A, Metall. Trans. A (1978) 587–593, https://doi.org/10.1007/BF02646416/METRICS.
[57] K. Sato, H. Sueyoshi, K. Yamada, Characterization of complex phase steel using backscattered electron images with controlled collection angles, Microscopy 64 (2015) 297–304, https://doi.org/10.1093/JMICRO/DFV022.